

# Growth characteristics of $\text{Ba}_x\text{Sr}_{(1-x)}\text{TiO}_3$ thin films produced by micro-arc oxidation

Min Wang<sup>1,a)</sup>, Xi Zuo<sup>2</sup>, Kang Li<sup>3</sup>, Kang Wang<sup>4</sup>, Guoge Zhang<sup>3</sup>

<sup>1</sup>College of Mechanical Engineering, Guangdong Polytechnic Normal University, Guangzhou 510635, China; and School of Materials Science and Engineering, South China University of Technology, Guangzhou 510641, China

<sup>2</sup>College of Mechanical Engineering, Guangdong Polytechnic Normal University, Guangzhou 510635, China

<sup>3</sup>School of Materials Science and Engineering, South China University of Technology, Guangzhou 510641, China

<sup>4</sup>College of Mechanical Engineering, DongGuan University of Technology, Dongguan 523808, China

<sup>a)</sup>Address all correspondence to this author. e-mail: wangmin@gpnu.edu.cn

Received: 7 October 2019; accepted: 5 March 2020

$\text{Ba}_x\text{Sr}_{(1-x)}\text{TiO}_3$  (BST) thin films were fabricated on a Ti substrate using micro-arc oxidation (MAO) in an aqueous solution with the addition of 0.6 M  $\text{Ba}(\text{OH})_2$ , 0.4 M  $\text{Sr}(\text{OH})_2$ , and 0.05 M EDTA. The morphology, composition, and electrical properties of BST films prepared under different processing times were characterized, and MAO growth characteristics of BST films were discussed. Results indicate that dielectric and ferroelectric properties of BST films are positively correlated with surface morphology dependent on MAO spark patterns. To obtain a smooth and compact film, the large spark stage should be avoided. During MAO processes, elements from the substrate and electrolyte solution migrate in opposite directions under an electric field, resulting in Ba, Sr, Ti, and O elements exhibiting a gradient distribution between the BST film and the Ti substrate. BST film prepared using MAO is composed of two layers: an outer loose layer and an inner dense layer. In addition, because of the position of discharge breakdown continually changing, the interface between the film and the substrate is uneven. As MAO processing time increases, BST film thickness increases and ferroelectric property improves. When processing time is 15 min, the residual polarization intensity (2Pr) of the BST film is about  $4.9 \mu\text{C}/\text{cm}^2$ .

## Introduction

$\text{Ba}_x\text{Sr}_{(1-x)}\text{TiO}_3$  ( $0 \leq x \leq 1$ , BST) is a complex perovskite material with a high and tunable dielectric constant and low dielectric loss. This compound has been extensively applied in the large-scale dynamic random memory [1, 2, 3, 4], nonvolatile ferroelectric memory [5, 6, 7], tunable microwave device [8, 9], and in many crucial optical components [6, 10, 11, 12]. Up to now, many techniques including magnetron sputtering [13, 14], sol-gel [15, 16, 17], pulsed laser deposition (PLD) [11, 18], and metal-organic chemical-vapor deposition (MOCVD) [19, 20] are commonly used to prepare fine dielectric films with tunable components. However, these technologies have their own advantages together with some drawbacks that limit the practical applications [21, 22, 23]. For instance, both magnetron sputtering and PLD can produce film with controllable components, but the film growth rate is low, and the cost of fabrication is high. Thus, it is difficult to obtain large membranes with good dielectric performance. The MOCVD can enhance the preparation efficiency, but the availability of some

pure and stable organic raw materials is always a tough problem. In addition, the solution for MOCVD process is usually highly toxic. The sol-gel process is deemed as a simple and cost-effective method for the preparation of large-sized ferroelectric membranes. However, microcracks might be produced during the subsequent heat-treatment process, leading to inferior ferroelectric performance. As a kind of surface modification techniques, micro-arc oxidation (MAO) can be used for the in situ preparation of ceramic coatings on the surfaces of some nonferrous metals. MAO has several advantages such as the fast rate of film deposition, simple operation, tunable film composition, strong adherence of the thin film with substrate, little pollution, and no need for post heat-treatment. Therefore, this technique is assigned as a technology with low cost and high efficiency for the preparation of the BST ferroelectric membranes with large area [24, 25, 26].

Since the 1990s, MAO has been applied in the preparation of functional films. Studies examining BST thin film prepared using MAO techniques have become extensive [27, 28, 29, 30],

with the majority of studies focusing on BST film preparation processes, its microstructure, and dielectric properties; few studies have examined growth processes and mechanisms of BST thin films prepared using MAO. In our study, MAO growth processes of BST film are investigated by analyzing the morphology, composition, and properties of BST films prepared using different processing times. It is hoped to obtain the growth mechanism of the BST film prepared using MAO technology, and a synthesis technology which can effectively prepare BST ferroelectric thin films with favorable microstructure and high performance at low cost will also be achieved.

## Results and discussion

### Surface morphology and composition of BST films

Results indicate that surface morphology of BST thin films differ as processing time increases (Fig. 1). When processing time is 2 min, MAO pores with a diameter  $\sim 250$  nm are evenly distributed on the surface, and the BST film is flat and dense. Surface roughness of the BST film is  $\sim 0.28$   $\mu\text{m}$  [Fig. 1(a)]. As processing time increases to 3 min, granules appear on the surface, resulting in surface roughness to increase to  $\sim 0.55$   $\mu\text{m}$ . Here, MAO pores begin to overlap, connect, and merge, resulting in larger pores of 300–600 nm [Fig. 1(b)]. When the processing time increases to 5 min, energy required for film discharge breakdown increases because of an increase in film thickness; the amount of molten oxide ejected also increases. As some molten oxides cannot quickly disperse, agglomerates are deposited on the surface of the BST film [Fig. 1(c)]. Surface roughness increases to  $\sim 0.52$   $\mu\text{m}$ . When the processing time increases to 10 min, the surface of the film is covered with volcanic protrusions, and surface roughness further increases to  $\sim 0.86$   $\mu\text{m}$ . The diameter of MAO pores increases to 2–5  $\mu\text{m}$  [Fig. 1(d)]. When the processing time increases to 15 min, volcanic nozzles disappear and surface roughness decreases to  $\sim 0.45$   $\mu\text{m}$  due to MAO pores filling with molten oxide; MAO pore diameter declines to 1–2  $\mu\text{m}$ . However, sinter and fusion of oxide in part of the surface on the film occur [Fig. 1(e)]. Finally, when the processing time is 20 min, a large number of particles are distributed on the surface of the film. This results in an uneven film surface, and surface roughness increases to  $\sim 0.61$   $\mu\text{m}$ . A number of cracks in the membrane are also recorded [Fig. 1(f)].

Surface morphology of BST films is closely related to the MAO spark pattern. During MAO processes, sparks changed in the following order (Fig. 2): Nonspark, white spark, orange spark, and big spark (arc break). In the no-spark stage, the surface of the Ti substrate was gradually passivated under the action of an electric field and electrolyte, and the metallic luster of the Ti substrate disappeared [Fig. 2(a)]. During this process, a large number of tiny bubbles began to dissipate from the

surface of both the cathode and anode. Noise recorded during this stage was virtually nonexistent. When the voltage increased to the breakdown value ( $V_B$ , 80 V), spark discharges occurred on the Ti surface. In the white spark stage, sparks were small, uniform, dense, and bright white [Fig. 2(b)]. This stage was accompanied by a slight crunching noise. When MAO entered into the orange spark stage [Fig. 2(c)], the number of sparks decreased, the size of sparks increased, and there was a sharp “squeak” sound. Finally, during the stage of big sparks, the number of sparks decreased, with the majority of sparks being mass-like and bright white [Fig. 2(d)]. The discharge reaction became very intense and bubbles mixed with electrolyte rush out of the liquid with a “crackling” sound, producing a white deposit at the interface between the Ti substrate and electrolyte.

In different spark discharge stages, because of the different discharge energy, the amount of molten oxide and the surface morphology of the BST film formed after spraying also differed. In the white spark stage, sparks were fine and uniform. As the initial oxide film was relatively uniform, a large number of discharge sparks were produced. The current and voltage between electrodes was low. Therefore, energy consumed by each discharge spark was very small, and molten oxide produced by discharge breakdown was also relatively small. The surface of the film was therefore smooth and dense. At the same time, because of the existence of pores and particles, inhomogeneity of the film increased, providing conditions for spark discharge in the next stage. In the orange spark stage, the number of sparks decreased and the size of sparks increased; voltage and current between electrodes also increased. Therefore, energy of a single discharge increased, and the amount of molten oxide ejected from the MAO discharge channels also increased, resulting in a volcanic nozzle on the surface of the film. Moreover, the surface of the film showed the characteristics of porous overlap due to repeated breakdown. When a large arc occurred, fine sparks on the film surface gradually disappeared. There were several persistent and strong discharges, resulting in defects such as sintering, cracks, or porosity. The longer the processing time, the longer the existence of the large arc, resulting in a rougher BST film surface. Therefore, to obtain a flat and dense BST film, the occurrence of large arcs should be avoided.

The distribution of the main elements in the BST film varies with treatment time (Fig. 3). When the processing time is less than 5 min, the overall distribution of Ba, Sr, Ti, and O in the film is uniform. When the processing time increases to 10 min, many large-sized black holes appear in the elements mapping. Compared with scanning electron microscope (SEM) results [Fig. 1(d)], volcano-like particles evident on the film surface are the main cause of black holes, and the distribution of elements in the film becomes more inhomogeneous as surface roughness increases. Surface roughness of the film

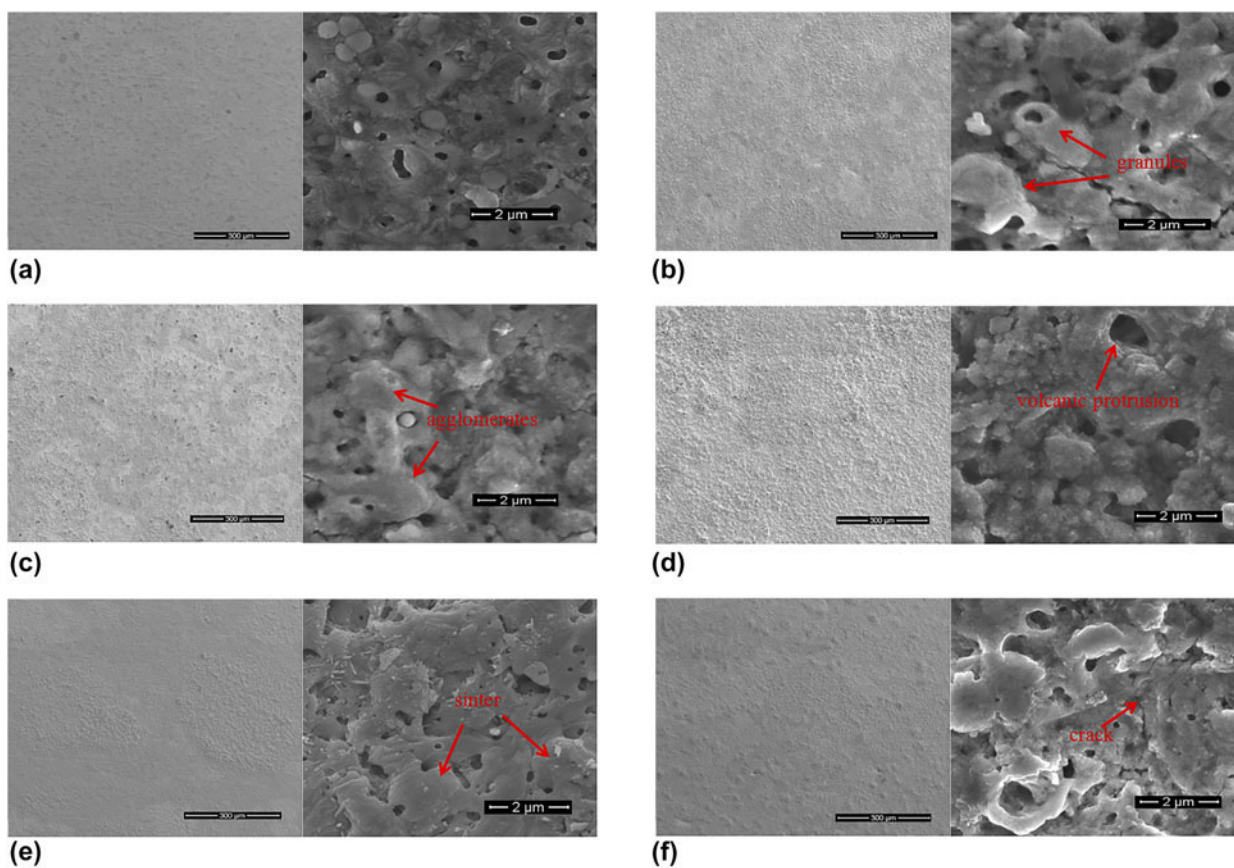


**Figure 1:** SEM micrographs of the BST films prepared under different processing times. (a) 2 min, (b) 3 min, (c) 5 min, (d) 10 min, (e) 15 min, and (f) 20 min.

decreases when processing time increases to 15 min [Fig. 1(e)]. Here, volcano-like particles decrease, and the uniformity of element distribution increases [Fig. 3(e)]. When treatment time increases to 20 min, volcano-like particles reappear, and cracks are recorded in the BST film [Fig. 1(f)], resulting in an increase in inhomogeneity of element distribution [Fig. 3(f)]. In conclusion, the distribution of Ba, Sr, Ti, and O in the BST membrane is closely related to the surface morphology of the BST film.

Variations in element information on the film are analyzed in a qualitative manner using X-ray photoelectrons spectroscopy (XPS) (Fig. 4). XPS spectra of the BST film obtained with the processing time of 5 min [Fig. 4(a)] records C to be present in the film, as well as Ba, Sr, Ti, and O. The high-resolution XPS spectra of C 1s, Ba 3d, Sr 3d, Ti 2p, and O 1s peaks are shown in Figs. 4(b)–4(f), respectively. The spectrum of C 1s [Fig. 4(b)] reveals two peaks with binding energies of 284.6 eV and 286.1 eV, respectively. The peak at 284.6 eV is assigned to adventitious C from the environment, and the peak at 286.1 eV is consistent with the binding energy of C in SrCO<sub>3</sub> and BaCO<sub>3</sub>. The Ba 3d spectrum [Fig. 4(c)] is composed of Ba 3d<sub>3/2</sub> (794.7 eV) and Ba 3d<sub>5/2</sub> peaks (779.4 eV), corresponding to the perovskite structure of BST. The Sr 3d spectrum [Fig. 4(d)]

records four peaks, with binding energies of 132.3, 133.8, 134.3, and 135.7 eV. The binding energy pair of 132.3 and 133.8 eV is assigned to Sr atoms in the perovskite phase; peaks at 134.3 and 135.7 eV are attributed to Sr atoms of carbonate. The Ti 2p XPS spectrum [Fig. 4(e)] is deconvoluted into two peaks (464.4 and 458.8 eV), corresponding to Ti 2p<sub>1/2</sub> and Ti 2p<sub>3/2</sub> peaks, respectively, with an energy interval of about 5.8 eV. The O 1s spectrum [Fig. 4(f)] can be fitted into two peaks, with binding energies of 532.4 and 530.3 eV. Although the peak at 532.4 eV is consistent with O 1s in SrCO<sub>3</sub> and BaCO<sub>3</sub>, it has a low content. The 530.3 eV peak is consistent with the binding energy of O atoms in TiO<sub>3</sub><sup>2-</sup>. In summary, the valence states of Ba, Sr, Ti, and O in the film are Ba<sup>2+</sup>, Sr<sup>2+</sup>, Ti<sup>4+</sup>, and O<sup>2-</sup>, respectively, and the membrane layer is mainly composed of tetragonal Ba<sub>x</sub>Sr<sub>(1-x)</sub>TiO<sub>3</sub> with a small amount of carbonate.

### Cross-section morphology and composition of BST films

Analysis of cross-section SEM images of BST-2, BST-3, BST-5, and BST-10 thin films indicates that, with a processing time of 2 min, a compact film with a thickness of about 2 μm is formed on the Ti substrate (Fig. 5). The interface between the film

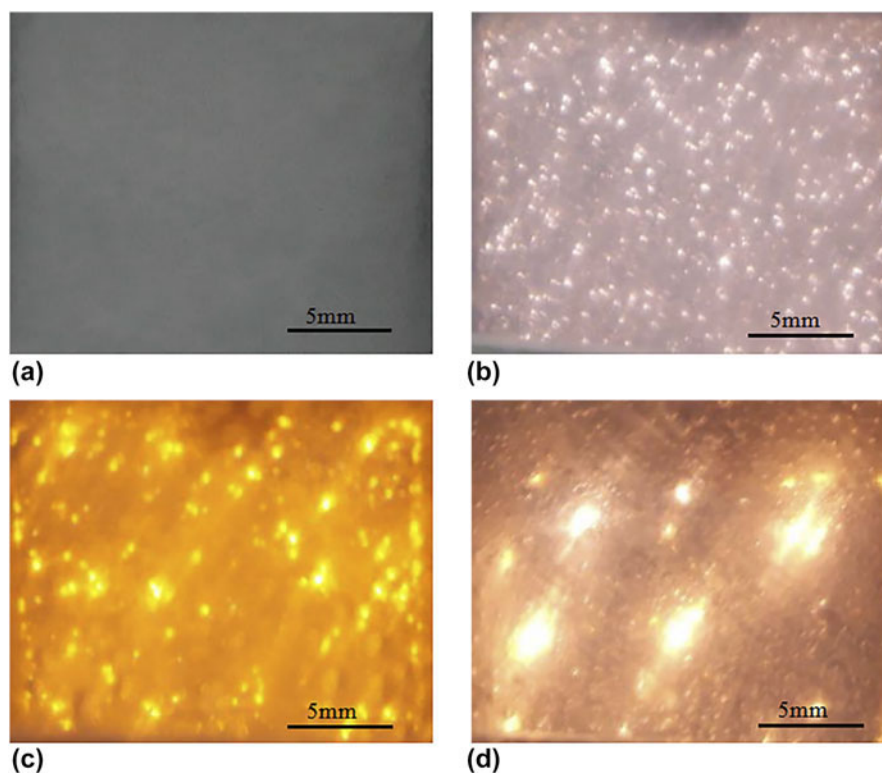


**Figure 2:** Electric spark formed during the process of MAO. (a) Nonspark, (b) white spark, (c) orange spark, and (d) big spark.

and the substrate is uneven, and the surface of the BST membrane is hilly. When processing time increases beyond 3 min, the BST film is obviously composed of two layers: an outer loose layer and an inner dense layer. In addition, the number and diameter of pores increase as processing time increases. MAO pores are only evident in the outer loose layer, and they do not traverse through the inner dense layer to the Ti substrate. Sparking always occurred on the thinner film where the film was easily broken down. Where cracks or pores were present on the dense layer, sparking occurred at these places, forming a discharge channel. Here, as fused oxide repaired the pores or cracks, no cracks or pores were identified in the dense layer [31, 32]. With the continuous generation of fused oxide, the thickness of the BST film increased, the location of the thinner film constantly changed, and the position of discharge breakdown also changed accordingly. These changes resulted in an uneven interface between the film and the substrate. A loose layer corresponding to the porous structure is recorded in the surface morphology (Fig. 1) of the BST films as granules with a loose porous structure.

To further examine MAO growth mechanisms of the BST thin film, electron probe microscopic analysis (EPMA) was undertaken on the cross section of the BST film (Fig. 6). Results indicate that, as processing time increases, Ti is continuously

diffused from the substrate to the film, and its distribution in the BST membrane is gradually homogenized. The content of O is basically unchanged, having an even distribution. As content in the membrane increases, Ba and Sr are uniformly distributed along the cross section. In general, when the processing time is greater than 5 min, the distribution of elements in the BST film is substantially uniform. EPMA results (Fig. 6) also indicate that a gradient distribution of Ba, Sr, O, and Ti between the BST film and the substrate is evident, indicating that the relative content of  $Ba_xSr_{(1-x)}TiO_3$  decreases and  $TiO_2$  increases from the coating surface to the Ti substrate. As Ba, Sr, and O elements mainly derive from the electrolyte, with Ti deriving from the substrate, during MAO processes, elements from the substrate and electrolyte migrate in opposite directions under an electric field. According to previous studies [33, 34], titanium was dissolved [Eq. (1)] and oxygen was evolved at the anode during the nonspark stage of MAO. Oxygen produced here could be dissolved in the electrolyte, producing  $O^{2-}$ , which reacted with  $Ti^{4+}$  to form titanium dioxide [Eq. (2)]. During the discharge breakdown of MAO,  $TiO_2$  should be continuously consumed to form a BST film [Eq. (3)], and new  $TiO_2$  was formed at the same time until MAO was completed. This indicated that the BST film grew inward and outward at the same time. Accordingly, the schematic figure of the



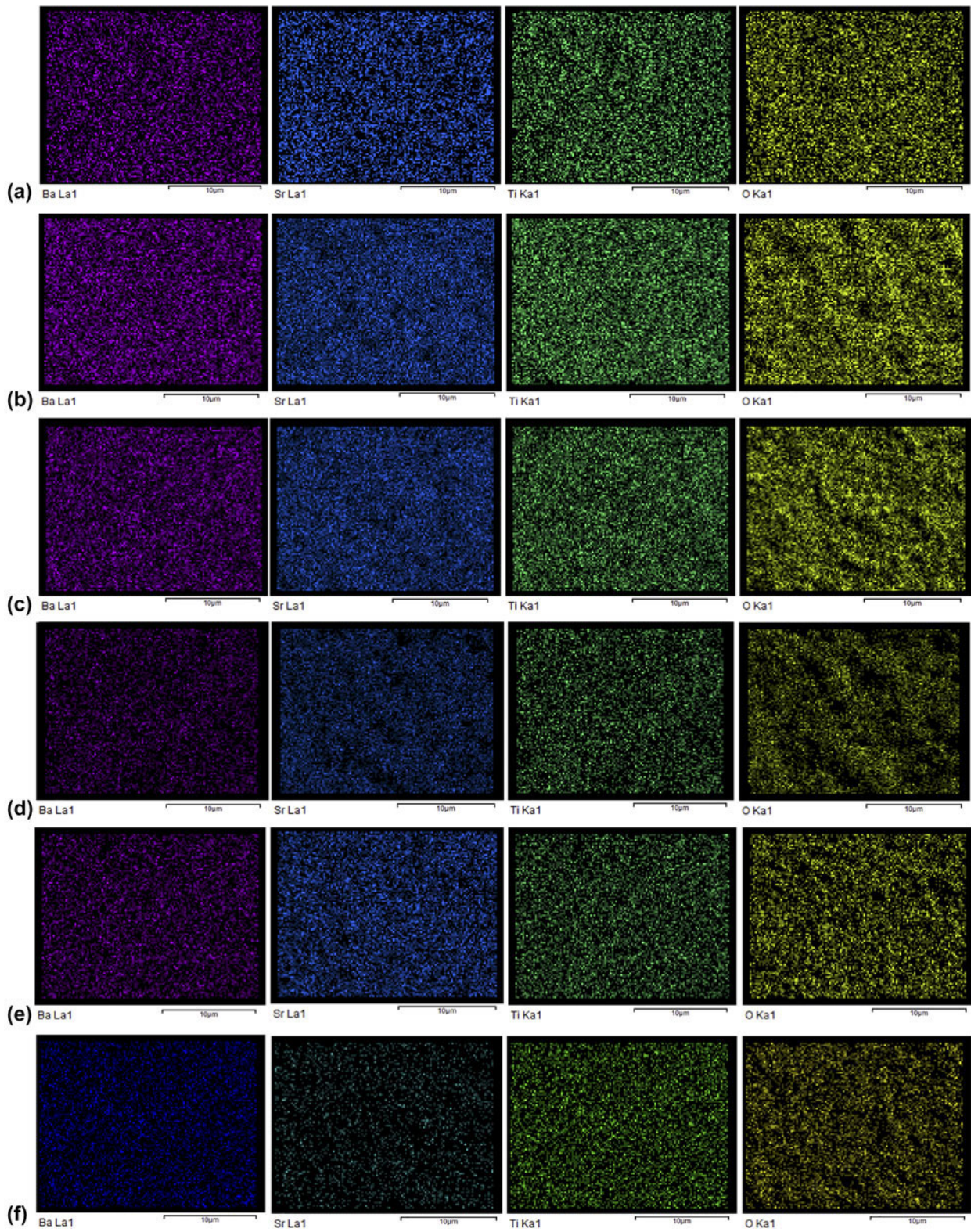


**Figure 3:** Elements mappings of the BST films prepared with different processing times. (a) 2 min, (b) 3 min, (c) 5 min, (d) 10 min, (e) 15 min, and (f) 20 min.



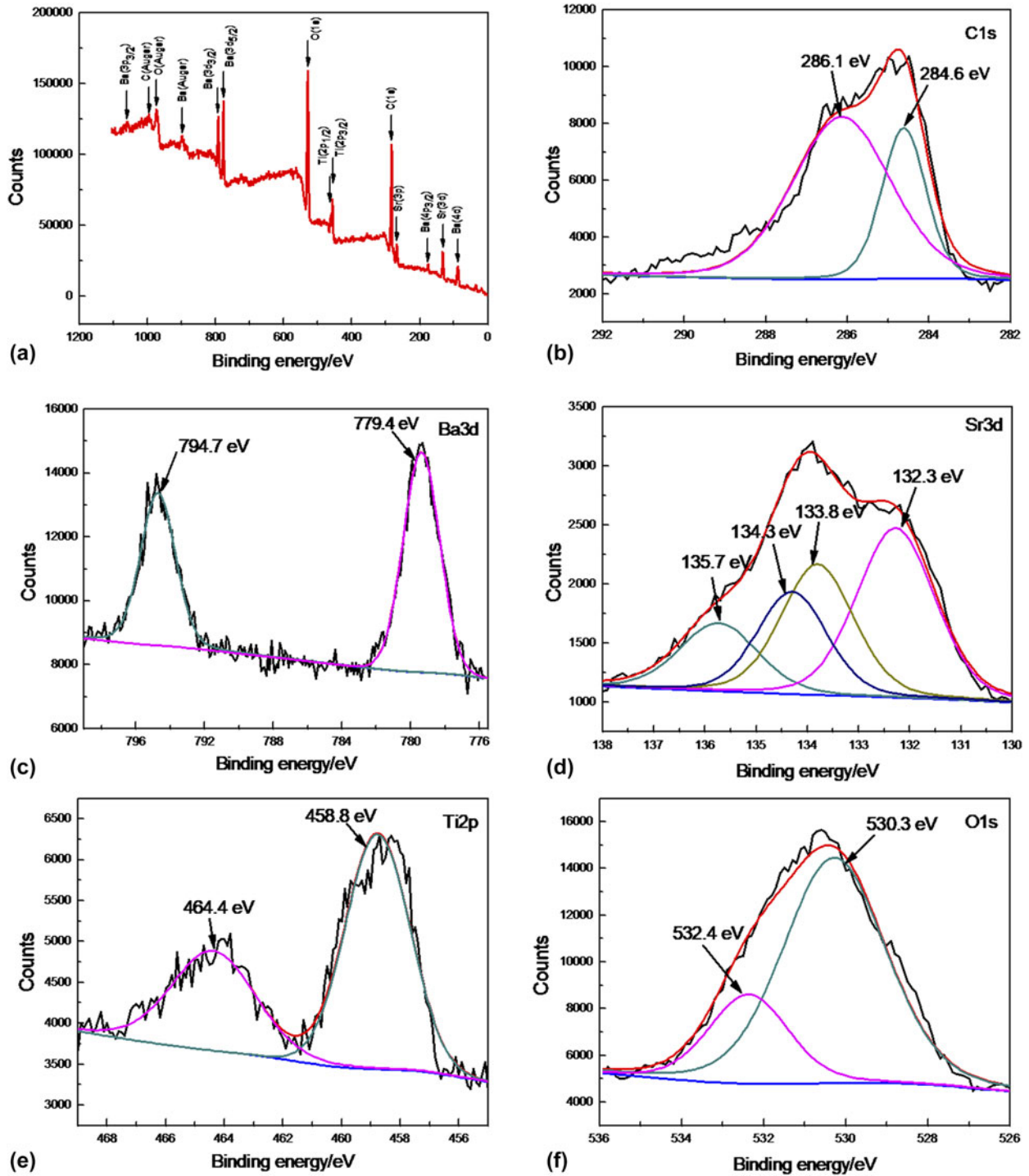
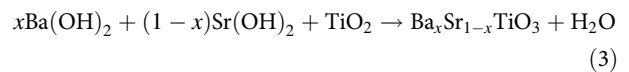
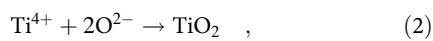
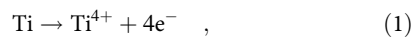
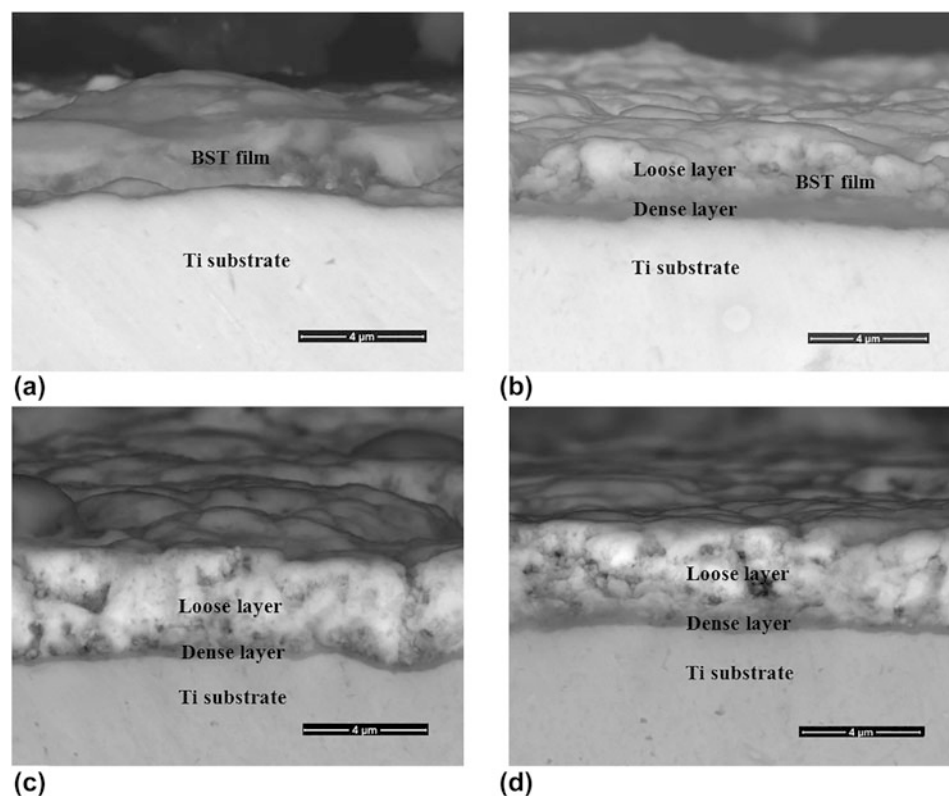


Figure 4: XPS spectra of the BST film. (a) Survey scan, (b) C 1s, (c) Ba 3d, (d) Sr 3d, (e) Ti 2p, and (f) O 1s.

formation of BST thin films prepared by MAO can be proposed (Fig. 7).



In addition, EPMA results (Fig. 6) indicate that O penetrates into the Ti substrate, this being a characteristic of MAO,



**Figure 5:** Cross-section SEM images of BST films prepared with different processing times. (a) 2 min, (b) 3 min, (c) 5 min, and (d) 10 min.

that is, penetration oxidation occurs. Because of the existence of penetration oxidation, a thick transition zone between the film and the substrate existed, resulting in a high adhesion of BST film [35, 36].

### Properties of the BST films

Dielectric constants and dielectric loss of BST films obtained at different processing times were analyzed at various frequencies (Fig. 8). Results show that BST films obtained at different times basically conform to the rule of high dielectric constant and low dielectric loss, except for BST-10. Combined with results in Fig. 1, the dielectric properties of BST films are positively correlated with the surface morphology of the films. Flat and dense BST film possesses a good dielectric property, and loose and rough BST film has an inferior dielectric property, such as BST-10.

The ferroelectric properties of BST films were tested at 500 V with a frequency of 200 Hz (Fig. 9). Results indicate that hysteresis loops of BST films gradually become slender, uniform, and symmetrical with an increase in processing time, indicating that the ferroelectric properties of BST films are continuously improving. When processing time is less than 3 min, the polarization intensity of the film decreases with an increase in voltage, and the hysteresis loop is in a state of “smiling mouth” [37, 38] [Figs. 9(a) and 9(b)]. The decline in residual polarization strength with an increase in voltage was

mainly attributed to oxygen vacancy in the membrane [39, 40, 41]. In the  $ABO_3$ -type oxides, oxygen atoms escaped from the lattice structure to form oxygen vacancies which pinned the inversion of the ferroelectric domains [42, 43]. With an increase in voltage, oxygen vacancies increased and the pinning effect on ferroelectric domains strengthened, thus ferroelectric domains could not be reversed in time, and the residual polarization strength of the films decreased. However, this phenomenon gradually decreases with time, and it is no longer evident when processing time exceeds 15 min. Moreover, according to Es-Souni [42], leakage current properties showed a strong dependence on thickness, and the space charge-limited current (SCLC) was advanced as a predominant conduction mechanism. In the SCLC mechanism, current density was dependent on voltage and thickness, as [44, 45]:

$$J = C \frac{V^n}{d^m} \quad (4)$$

where  $J$  is the current density,  $d$  is the BST film thickness,  $V$  is the operation voltage, and  $C$ ,  $n$ , and  $m$  are arbitrary constants. This equation shows that when the thickness of the ferroelectric film increases, leakage current decreases. At the same time, the ferroelectric property of the film improves. By combining Eq. (4) and Fig. 6, it can be seen that with an increase in

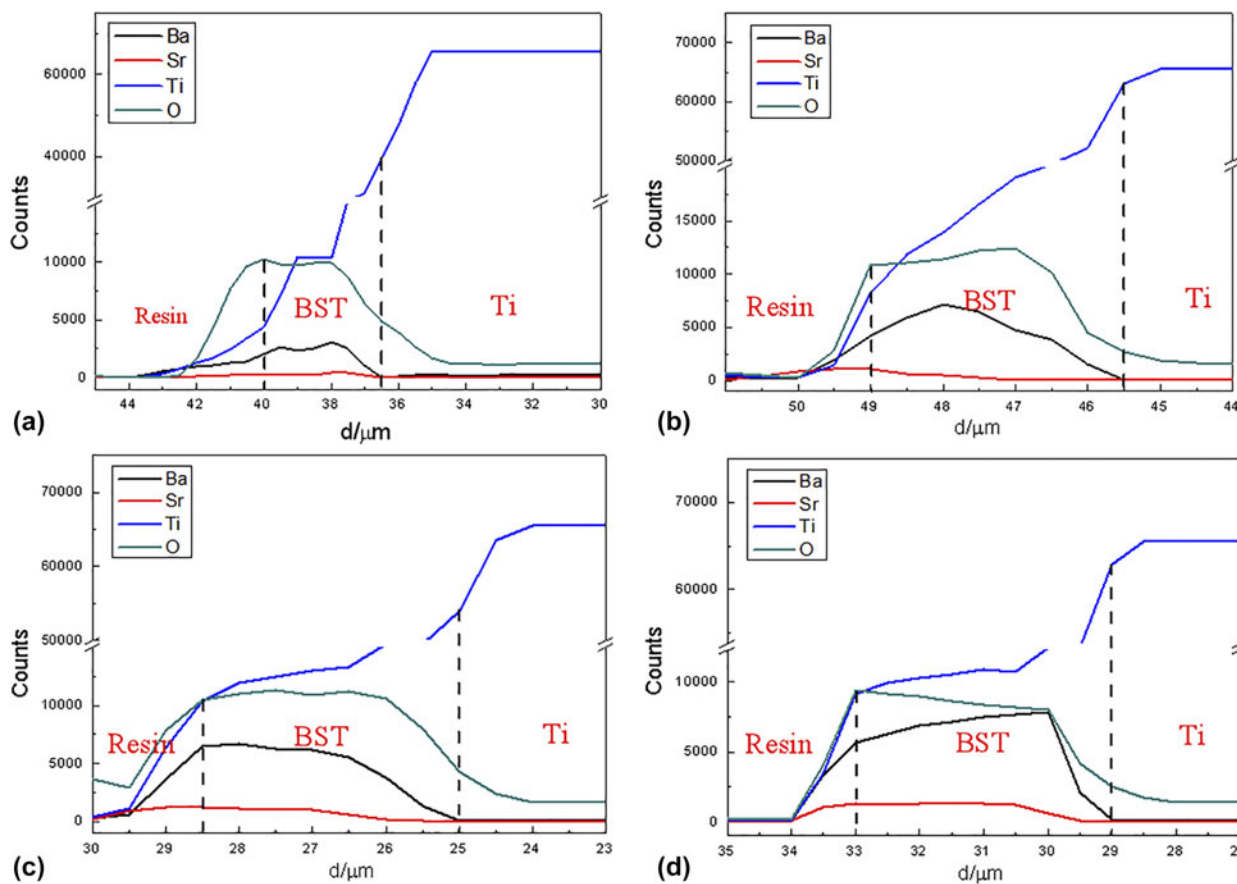


Figure 6: EPMA results of BST thin films obtained under different processing times. (a) 2 min, (b) 3 min, (c) 5 min, and (d) 10 min.

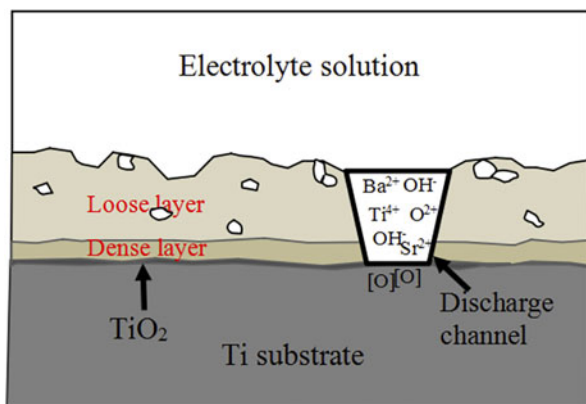


Figure 7: Schematic diagram of the formation of BST thin film prepared by micro-arc oxidation.

processing time, film thickness increases, leakage current decreases, and the ferroelectric property of the BST thin film is enhanced: findings that are consistent with those in Fig. 9. In addition, dielectric and ferroelectric properties of BST thin films were closely related to the film microstructure [46]. With a reduction of the film surface roughness and improvement of film density, the capacitance of the film increased and ferroelectric performance was optimized because of a decrease

in mismatch stress and a reduction in the nonperovskite structure [43, 47]. Results in Fig. 8(e) indicate that the positive residual polarization intensity ( $P_r$ ) and negative residual polarization intensity ( $-P_r$ ) of the BST film obtained after 15 min are about  $2.4 \mu\text{C}/\text{cm}^2$  and  $-2.5 \mu\text{C}/\text{cm}^2$ , respectively. The positive coercive voltage is about 160 V, and the negative coercive voltage is about  $-190 \text{ V}$ .

## Conclusion

In this study, growth characteristics of MAO in BST films were identified by analyzing morphology, composition, and properties of BST films under different processing times. Results indicated that the final surface morphology of the BST film was closely related to the MAO spark pattern. To obtain a smooth and compact film, a large spark stage should be avoided. BST film prepared using MAO technique was composed of two layers: an outer loose layer and an inner dense layer. When processing time was greater than 5 min, the distribution of Ba, Sr, Ti, and O in the BST film was substantially uniform, and a gradient distribution of Ba, Sr, O, and Ti existed between the BST film and the substrate. The dielectric properties of BST films were positively correlated with surface



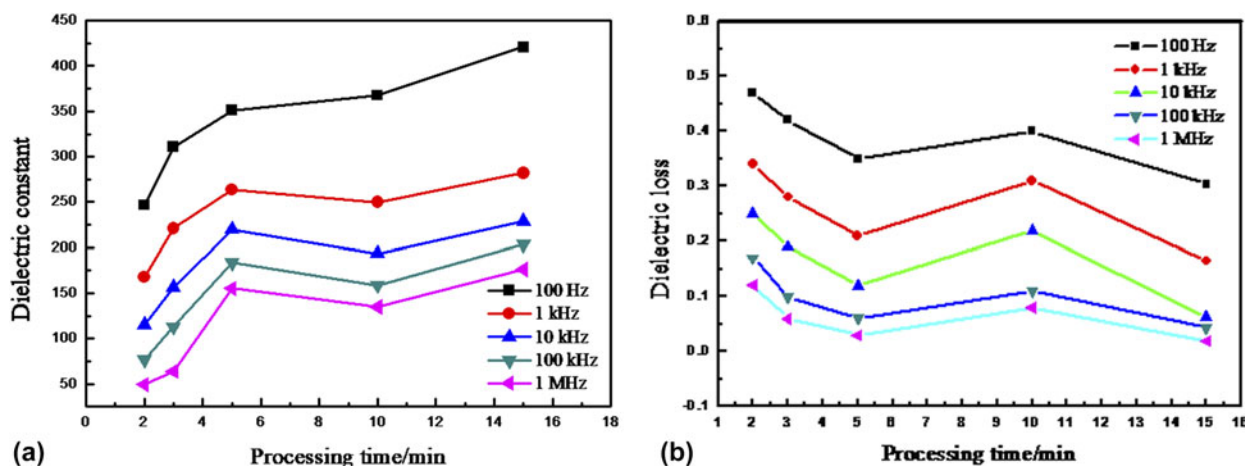


Figure 8: (a) Dielectric constants and (b) dielectric loss of the BST thin films prepared with different processing times.

morphology; flat and dense BST film possesses a good dielectric property. Results from our study provide new findings and reference values for low-cost preparation of high-performance BST films.

## Experimental methods

### BST samples preparation

Ti 99.6% (Guangzhou Changcheng Titanium Co., Ltd., China) with a dimension of  $40 \times 20 \times 2 \text{ mm}^3$  was used as the substrate for the preparation of BST membrane. The titanium sheet was grounded by SiC paper with different grits from 180 to 1000. After grinding, the titanium substrates were subjected to an acid pickling in a mixed solution of 25% HF and 75% HNO<sub>3</sub> by volume, followed by rinsing with anhydrous acetone and distilled water. The samples were then dried with hot air. The MAO process was conducted by using a JYW-50 series equipment (Guangzhou Jingyuan Electronic Equipment Company, China). The titanium plate was applied as the anode, and a 304 stainless steel was used as the cathode. An aqueous solution of 0.6 M Ba(OH)<sub>2</sub>, 0.4 M Sr(OH)<sub>2</sub>, and 0.05 M EDTA was used as the electrolyte. Temperature of the electrolyte was controlled at 50–60 °C by a water-cooling system. The current density and frequency were set as 0.5 A/cm<sup>2</sup> and 150 Hz, respectively, and the duty ratio of MAO process was 80%. Processing times were set as 2 min, 3 min, 5 min, 10 min, 15 min, and 20 min, respectively. For the convenience of expression, BST-*n* (*n* refers to processing time) was used hereafter.

### Characterizations

The surface and cross-section morphology of the BST films were characterized using an FEI Nava-Nano 430 SEM, operated at 20 KV. The cross-section samples were prepared using the following method. Fresh cross-section samples of the BST

films were initially cut using a BUEHLER IsoMet 5000 cutter, and then the samples were inlaid using a BUEHLER Isimpli-Met 3000 metallographic inlay machine. Before observation and analyses, the samples were sanded using SiC paper successively up to 1500 grit before being polished with a diamond polishing fluid (3 μm) and an aluminum trioxide polishing fluid (0.02 μm), respectively. Finally, the samples were rinsed with deionised water and air-dried. To reveal the fine microstructure, the samples were plated with Au using a Leica EM SCD 500 device. Energy dispersive spectrometer (EDS) attached to SEM was used to detect elemental composition and distribution of the BST thin films. Surface roughness of the BST thin film was measured using a German BMT Exert 3D tomography. Each sample was measured horizontally and vertically at three different positions with a scan length of 10 mm, and average surface roughness was recorded. XPS incorporating a Kratos Ultra Axis spectrometer equipped with a monochromatized Al-K<sub>α</sub> X-ray source (1486.6 eV) was used to analyze the chemical composition of the BST membrane and the binding states. The electron analyzer was used in a constant analyzer energy mode using a full and a narrow spectral-pass energy of 160 and 40 eV, respectively. Peak analyses were performed using the XPS Peak 41 Software. The energy scale was calibrated by assigning the energy of 284.6 eV to the C 1s peak, corresponding to the adventitious carbon. The cross-section composition of BST membrane was characterized by an electron probe X-ray microanalyzer (Shimadzu, EPMA-1600). The impedance analyzer (Agilent HP4284) was applied for testing the electric capacity and dielectric loss value. The testing voltage was 1.0 V with the frequency ranged from 20 to  $1 \times 10^6$  Hz. The polarization versus electric field (*P*-*E*) hysteresis characteristics were obtained using a Radiant Precision LC material analyzer. Before testing, a Pt electrode was deposited on the BST membrane using a Leica EM SCD 500 device. The

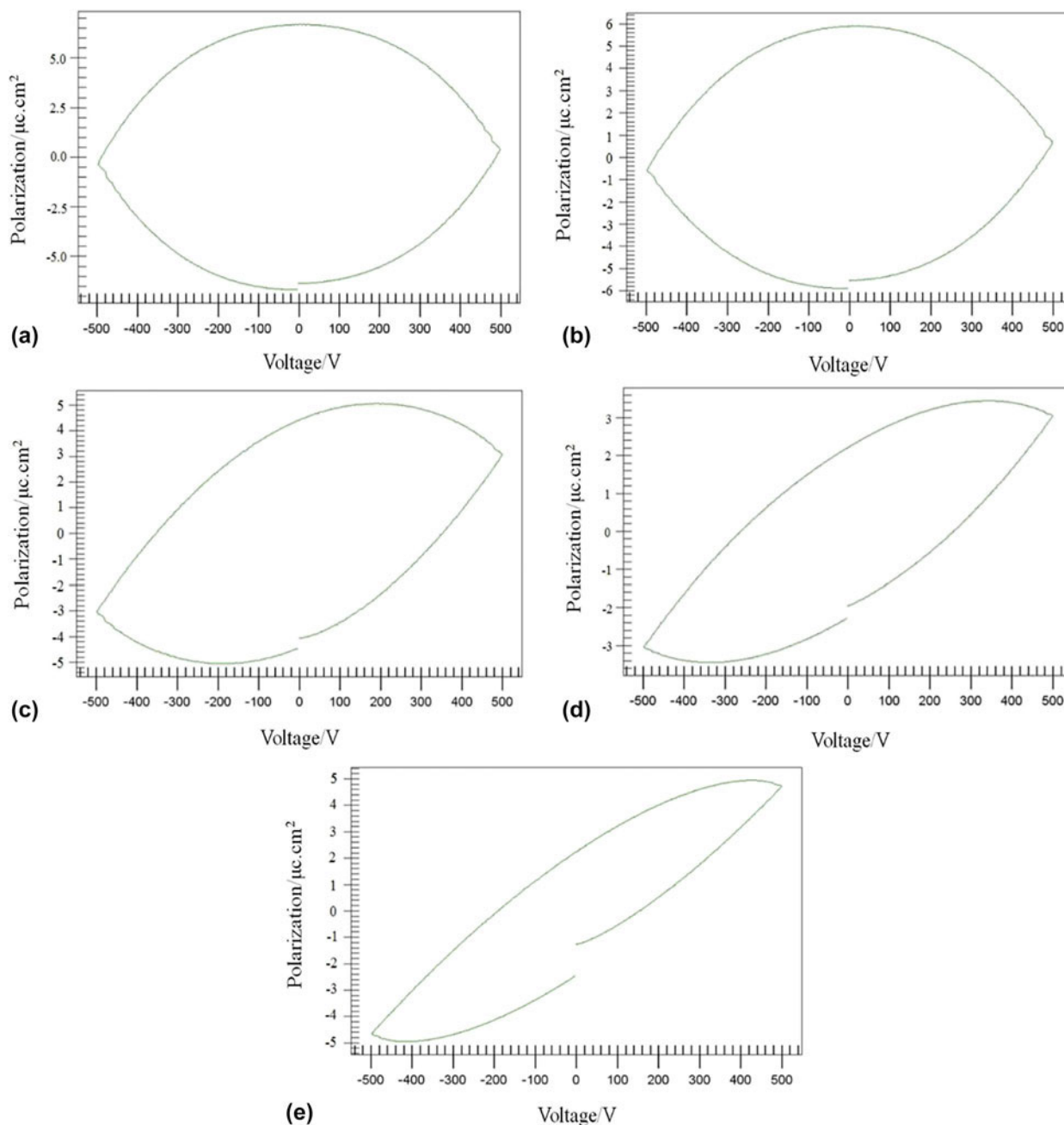


**Figure 9:** Electric hysteresis loops of the BST thin films with different processing times. (a) 2 min, (b) 3 min, (c) 5 min, (d) 10 min, and (e) 15 min.

dielectric constants of the thin films were calculated according to  $\epsilon' = C \cdot d / (S \cdot \epsilon_0)$ , where  $d$  is the thickness of the BST film,  $\epsilon'$  is the dielectric constant,  $C$  is the electric capacity of the sample, and  $S$  is the area of the electrode ( $0.785 \text{ cm}^2$ ). The dielectric constant in a vacuum,  $\epsilon_0$ , is  $8.85 \times 10^{-12} \text{ F/m}$ .

## Acknowledgments

This study was supported by the Science and Technology Planning Project of Guangdong Province (No. 2016A010103040)

and the Educational Commission of Guangdong Province (No. 2015KTSCX084).

## References

1. **Irzaman, M. Dahrul, B. Yulianto, K.A. Hammam, and H. Alatas:** Effects of Li and Cu dopants on the crystal structure of  $\text{Ba}_{0.65}\text{Sr}_{0.35}\text{TiO}_3$  thin films. *Ferroelectrics Lett.* **45**, 49 (2018).
2. **R. Dewi:** Formation and characterization of typical films  $\text{Ba}_{0.2}\text{Sr}_{0.8}\text{TiO}_3$  using XRD, FESEM, and spectroscopy impedance. *J. Phys.: Conf. Ser.* **1120**, 012009 (2018).

3. **R.B. Upadhyay, K. Jalaja, and U.S. Joshi:** Structural and electrical properties of Ba<sub>0.6</sub>Sr<sub>0.4</sub>TiO<sub>3</sub> thin film on LNO/Pt bottom electrode. *AIP Conf. Proc.* **1837**, 030001 (2017).
4. **C. Liu and P. Liu:** Microstructure and dielectric properties of BST ceramics derived from high-energy ball-milling. *J. Alloys Compd.* **584**, 114–118 (2014).
5. **E.K. Palupil, R. Umam, B.B. Andriana, H. Sato, B. Yulianto, H. Alatas, and Irzaman:** Micro-Raman spectroscopy investigation of chlorophyll-doping effects on Ba<sub>0.2</sub>Sr<sub>0.8</sub>TiO<sub>3</sub> thin film. *J. Phys.: Conf. Ser.* **1155**, 012044 (2019).
6. **R.R. Romanofsky and R.C. Toonen:** Past, present, and future of ferroelectric and multiferroic thin films for array antennas. *Multidimens. Syst. Signal Process.* **29**, 475–487 (2018).
7. **P. Singh, P.K. Rout, M. Singh, R.K. Rakshit, and A. Dogra:** Ferroelectric memory resistive behavior in BaTiO<sub>3</sub>/Nb doped SrTiO<sub>3</sub> heterojunctions. *Thin Solid Films* **643**, 60–64 (2017).
8. **N. Kevin, C. Borderon, R. Renoud, A. Ghalem, A. Crunteanu, L. Huitema, F. Dumas-Bouchiat, P. Marchet, C. Champeaux, and H.W. Gundel:** Diffuse phase transition of BST thin films in the microwave domain. *Appl. Phys. Lett.* **112**, 262901 (2018).
9. **L. Lai, Y. Xu, Y. Ren, H. Gao, X. Wang, J. Zhu, Y. He, and X. Zhu:** Low loss and highly tunable (Ba,Sr)(Ti,Mn)O<sub>3</sub>/(Ba,Sr)TiO<sub>3</sub> bilayered films for electrically tunable microwave device applications. *J. Mater. Sci.: Mater. Electron.* **28**, 5718–5724 (2017).
10. **E.K. Palupi, H. Alatas, and Irzaman:** Analysis of energy gap and the refractive index of barium strontium titanate (Ba<sub>0.2</sub>Sr<sub>0.8</sub>TiO<sub>3</sub>) films doped of chlorophyll from green leafy vegetables. *IOP Conf. Ser. Earth Environ. Sci.* **209**, 012012 (2018).
11. **B. Vigneshwaran, P. Kuppusami, A. Panda, A. Singh, and H. Sreemoolanadhan:** Microstructure and optical properties of Ba<sub>0.6</sub>Sr<sub>0.4</sub>TiO<sub>3</sub> thin films prepared by pulsed laser deposition. *Mater. Res. Express* **5**, 066420 (2018).
12. **M. Bordbari, M.J. Eshraghi, N. Naderi, and A.S.A.H. Zadeh:** Investigation of structural and optical properties of oblique angle sputter deposited barium strontium titanate nanostructures. *Mater. Res. Express* **6**, 025009 (2018).
13. **K. Rachut, J. Thorsten, M. Bayer, and J.O. Wolff, B. Kmet, A. Benčan, and A. Klein:** Off-stoichiometry of magnetron sputtered Ba<sub>1-x</sub>Sr<sub>x</sub>TiO<sub>3</sub> thin films. *Phys. Status Solidi B* **256**, 1900148 (2019).
14. **F.W. Jamaluddin, M.F. Abdul Khalid, M.H. Mamat, A.S. Zoolfakar, M.A. Zulkefle, M. Rusop, and Z. Awang:** Characterization of barium strontium titanate thin films on sapphire substrate prepared via RF magnetron sputtering system. *AIP Conf. Proc.* **1963**, 020065 (2018).
15. **N. Abu Bakar, J. Adnan, R.A.M. Osman, Z.A.Z. Jamal, M.A. Idris, and W.M.F. Wan Nik:** Sol gel preparation methods for barium strontium titanate based solar devices. *Phys. Status Solidi* **2068**, 020057 (2019).
16. **P. Ge, X. Tang, Q. Liu, Y. Jiang, W. Li, and J. Luo:** Energy storage properties and electrocaloric effect of Ba<sub>0.65</sub>Sr<sub>0.35</sub>TiO<sub>3</sub> ceramics near room temperature. *J. Mater. Sci.: Mater. Electron.* **29**, 1075–1081 (2018).
17. **A. Elbasset, S. Sayouri, F. Abdi, T. Lamcharfi, and L. Mrharrab:** Effect of Sr addition on piezoelectric properties and the transition temperature of BaTiO<sub>3</sub>. *Glass Phys. Chem.* **43**, 91–97 (2017).
18. **J. Pundareekam Goud, M.S. Alkathy, K. Sandeep, S. Ramakanthand, and K.C. James Raju:** Influence of laser fluence on structural, optical, and microwave dielectric properties of pulsed laser deposited Ba<sub>0.6</sub>Sr<sub>0.4</sub>TiO<sub>3</sub> thin films. *J. Mater. Sci.: Mater. Electron.* **29**, 15973 (2018).
19. **M. Reinke, Y. Kuzminykh, F. Eltes, S. Abel, T. LaGrange, A. Neels, F. Jean, and P. Hoffmann:** Low temperature epitaxial barium titanate thin film growth in high vacuum CVD. *Adv. Mater. Interfaces* **4**, 1700116 (2017).
20. **K. Yoshiizumi, T. Tai, M. Nishide, H. Shima, H. Funakubo, K. Nishida, and T. Yamamoto:** Growth and evaluation of epitaxial BaTiO<sub>3</sub> thin films of less than 100 nm thickness by metal-organic chemical vapor deposition. *Jpn. J. Appl. Phys.* **54**, 035501 (2015).
21. **D. Yan, L. Luo, Y. Zhang, Z. Peng, H. Liu, D. Xiao, T. Liu, X. Lai, and J. Zhu:** Influence of deposition temperature on microstructure and electrical properties of modified (Ba,Sr)TiO<sub>3</sub> ferroelectric thin films. *Ceram. Int.* **41**, S520–S525 (2015).
22. **S. Xiao, W. Jiang, K. Luo, H.X. Jin, and Z. Lin:** Structure and ferroelectric properties of barium titanate films synthesized by sol–gel method. *Mater. Chem. Phys.* **127**, 420–425 (2011).
23. **G. Shuster, O. Kreinin, E. Lakin, N.P. Kuzmina, and E. Zolotoyabko:** MOCVD growth of barium-strontium titanate films using newly developed barium and strontium precursors. *Thin Solid Films* **518**, 4658–4661 (2010).
24. **M. Tezuka and M. Iwasaki:** Plasma-induced degradation of aniline in aqueous solution. *Thin Solid Films* **386**, 204–207 (2001).
25. **Y-K. Shin, W-S. Chae, Y-W. Song, and Y-M. Sung:** Formation of titania photocatalyst films by microarc oxidation of Ti and Ti–6Al–4V alloys. *Electrochem. Commun.* **8**, 465–470 (2006).
26. **M-H. Hong, D-H. Lee, K-M. Kim, and Y-K. Lee:** Study on bioactivity and bonding strength between Ti alloy substrate and TiO<sub>2</sub> film by micro-arc oxidation. *Thin Solid Films* **519**, 7065–7070 (2011).
27. **S.V. Gnednikov, P.S. Gordienko, O.A. Khrisanfova, T.M. Scorobogatova, and S.L. Sinebrukhov:** Formation of BaTiO<sub>3</sub> coatings on titanium by microarc oxidation method. *J. Mater. Sci.* **37**, 2263–2265 (2002).
28. **C. Wu and F. Lu:** Synthesis of barium titanate films by plasma electrolytic oxidation at room electrolyte temperature. *Surf. Coating. Technol.* **199**, 225–230 (2005).
29. **J. Peng, B. Han, W. Li, J. Du, P. Guo, and D. Han:** Study on the microstructural evolution of BaTiO<sub>3</sub> on titanium substrate during MAO. *Mater. Lett.* **62**, 1801–1804 (2008).



30. **W. Huang, W. Li, and B. Han:** Study on BaTiO<sub>3</sub> films prepared by AC power microarc oxidation. *Sci. China, Ser. E: Technol. Sci.* **52**, 2195–2199 (2009).
31. **H.F. Guo, M.Z. An, H.B. Huo, S. Xu, and L.J. Wu:** Microstructure characteristic of ceramic coatings fabricated on magnesium alloys by micro-arc oxidation in alkaline silicate solutions. *Appl. Surf. Sci.* **252**, 7911–7916 (2006).
32. **Z. Zhao, Q. Pan, J. Yan, J. Ye, and Y. Li:** Direct current micro-arc oxidation coatings on Al–Zn–Mg–Mn–Zr extruded alloy with tunable structures and properties templated by discharge stages. *Vacuum* **50**, 155–165 (2018).
33. **J. Schreckenbach, F. Schlottig, G. Marx, W.M. Kriven, O.O. Popoola, M.H. Jilavi, and S.D. Brown:** Preparation and microstructure characterization of anodic spark deposited barium titanate conversion layers. *J. Mater. Res.* **14**, 1437–1443 (1999).
34. **A.L. Yerokhin, N. Xie, A. Leyland, A. Matthews, and S.J. Dowey:** Plasma electrolysis for surface engineering. *Surf. Coating. Technol.* **122**, 73–93 (1999).
35. **Q. Li, W. Yang, C. Liu, D. Wang, and J. Liang:** Correlations between the growth mechanism and properties of micro-arc oxidation coatings on titanium alloy: Effects of electrolytes. *Surf. Coating. Technol.* **316**, 162–170 (2017).
36. **W. Tang, J. Yan, G. Yang, G. Gan, J. Du, J. Zhang, Y. Liu, Z. Shi, and J. Yi:** Effect of electrolytic solution concentrations on surface hydrophilicity of micro-arc oxidation ceramic film based on Ti6Al4V titanium alloy. *Rare Met. Mater. Eng.* **43**, 2883–2888 (2014).
37. **Y. Chen, Z. Pen, Q. Wang, and J. Zhu:** Crystalline structure, ferroelectric properties, and electrical conduction characteristics of W/Cr Co-doped Bi<sub>4</sub>Ti<sub>3</sub>O<sub>12</sub> ceramics. *J. Alloys Compd.* **612**, 120–125 (2014).
38. **R. Sankar Ganesh, S.K. Sharma, N. Abinnas, E. Durgadevi, P. Raji, S. Ponnusamy, C. Muthamizhchelvan, Y. Hayakawa, and D.Y. Kim:** Fabrication of the flexible nanogenerator from BTO nanopowders on graphene coated PMMA substrates by sol–gel method. *Mater. Chem. Phys.* **192**, 274–281 (2017).
39. **M.S. Tsai, S.C. Sun, and T.Y. Tseng:** Effect of oxygen to argon ratio on properties of (Ba,Sr)TiO<sub>3</sub> thin films prepared by radio-frequency magnetron sputtering. *J. Appl. Phys.* **82**, 3482–3487 (1997).
40. **M. Shen, Z. Dong, Z. Gan, and S. Ge:** Oxygen-related dielectric relaxation and leakage characteristics of Pt/(Ba,Sr)TiO<sub>3</sub>/Pt thin-film capacitors. *Appl. Phys. Lett.* **80**, 2538–2540 (2002).
41. **C.H. Park and D.J. Chadi:** Microscopic study of oxygen-vacancy defects in ferroelectric perovskites. *Phys. Rev. B* **57**, 961–964 (1998).
42. **S. Ezhilvalavan and T-Y. Tseng:** Progress in the developments of (Ba,Sr)TiO<sub>3</sub>(BST) thin films for Gigabit era DRAMs. *Mater. Chem. Phys.* **65**, 227–248 (2000).
43. **J.X. Liao, C.R. Yang, Z. Tian, H.G. Yang, and L. Jin:** The influence of post-annealing on the chemical structures and dielectric properties of the surface layer of Ba<sub>0.6</sub>Sr<sub>0.4</sub>TiO<sub>3</sub> films. *J. Phys. D: Appl. Phys.* **39**, 2473 (2006).
44. **M. Es-Souni, N. Zhang, S. Iakovlev, C-H. Solterbeck, and A. Piorra:** Thickness and erbium doping effects on the electrical properties of lead zirconate titanate thin films. *Thin Solid Films* **440**, 26–34 (2003).
45. **J.C. Shin, C.S. Hwang, H.J. Kim, and S.O. Park:** Leakage current of sol–gel derived Pb(Zr,Ti)O<sub>3</sub> thin films having Pt electrodes. *Appl. Phys. Lett.* **75**, 3411 (1999).
46. **X.Z. MinWang, W. Li, G. Cao, and A. Xiang:** Enhanced dielectric performance of Ba<sub>x</sub>Sr<sub>(1-x)</sub>TiO<sub>3</sub> films prepared by the direct current micro-arc oxidation in the presence of ethylenediamine tetraacetic acid. *Thin Solid Films* **694**, 137579 (2020).
47. **Z. Saroukhani, N. Tahmasebi, S.M. Mahdavi, and N. Ali:** Effect of working pressure and annealing temperature on microstructure and surface chemical composition of barium strontium titanate films grown by pulsed laser deposition. *Bull. Mater. Sci.* **38**, 1645–1650 (2015).